3-D Analysis and Experimental Verification of A Novel Magnetic Lead Screw with Checkerboard Array Magnetic Pole

SCHOLARONE™
Manuscripts

1
2   1
3
4
5
3-D Analysis and Experimental Verification of A Novel Magnetic Lead Screw with Checkerboard Array Magnetic Pole

Lixun Zhu, Hao Ji, Runhua Fan, Ting Xu, Ning Gao, Kangan Wang, Min Huang, Xinglong Jin, Wei Li, *Member*, *IEEE*, Chang-seop Koh, *Senior Member, IEEE* and Frede Blaabjerg, *Fellow, IEEE*

Abstract—In this paper, a novel checkerboard array pole (CAP) magnetic lead screw (MLS) is proposed. Compared with the traditional MLS, the proposed CAP-MLS can not only save permanent magnet (PM) consumption but also provide enough thrust for application. To save PM consumption, permanent magnet (PM) and iron teeth are alternately mounted to form a circle of helical magnetic poles on the mover of the proposed CAP-MLS. Meanwhile, the traditional pure PM helical poles are mounted on the rotor to increase the maximum thrust and torque. On the other hand, a three-dimensional (3-D) analytical model based on the superposition theory for the proposed CAP-MLS is established to analyse and predict the magnetic field distribution in airgap, thrust force, and torque. The analytical results are compared with those from a 3-D finite element analytical model and experimental prototype to verify the effectiveness of the proposed novel topology and its corresponding 3-D analytical model.
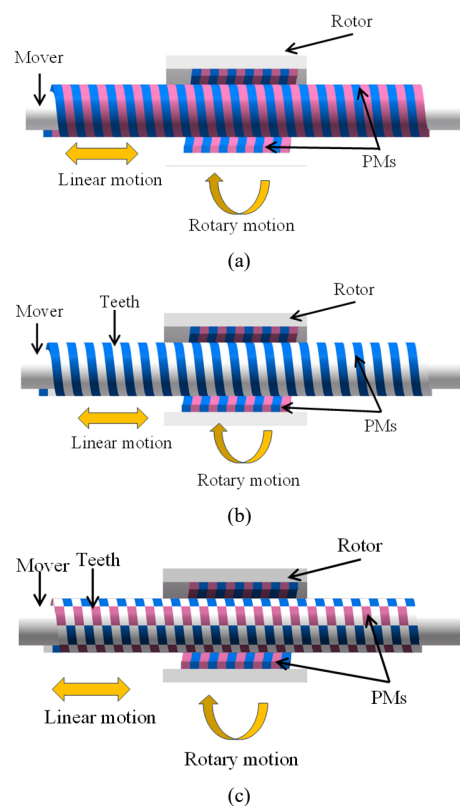
***Index Terms*—Subdomain analytical model, magnetic lead screw, magnetic screw.**

I. INTRODUCTION

MAGNETIC lead screw (MLS) is an electromagnetic device that can transfer the linear and rotary motion of each other. It consists of a mover and a rotor; the rotor can be clockwise and counterclockwise rotational, driven by the forward and backward motion of the mover through the helical coupling magnetic field in the air gap, and vice versa. Compared with the traditional mechanical lead screw, the MLS has the advantages of simple structure, smooth operation, long life, high reliability, and low-frequency maintenance precise movement. MLS can be widely used

instead of the mechanical lead screw used in energy harvesting, medical devices, aerospace, and other fields [1]-[5]. With the continuous progress of permanent magnet (PM) performance, MLS research is also developing. Although magnetic screws have many advantages, due to the material properties of the limitations of the manufacturing and installation process in the existence of challenge.

So far, several MLS topology types have been proposed and investigated, including conventional MLS, reluctance MLS, excited MLS, consequent-pole (CP) MLS, segmented modulated MLS [6]-[11], and so on. Because the effective operating region of MLS depends on the length of the rotor, and the length of the mover is much longer than the rotor. CP-MLS is considered one of the most PM consumption performances among all MLSes. However, the symmetric

Lixun Zhu, Hao Ji, Ting Xu, Ning Gao, Kangan Wang, and Min Huang are with the Department of Electrical Engineering, Shanghai Maritime University, Shanghai 201306, China (e-mail: lixzhu@shmtu.edu.cn; 202330210237@stu.shmtu.edu.cn; ting.x@wustl.edu; ngao@shmtu.edu.cn; kawang@shmtu.edu.cn; minhuang@shmtu.edu.cn)

Runhua Fan are with the College of Ocean Science and Engineering, Shanghai Maritime University, Shanghai 201306, China (e-mail: rhfan@shmtu.edu.cn)

Xinglong Jin is with the Taiyuan Heavy Industry(Shanghai) Equipment Technology Co., Ltd. (email: 540293023@qq.com)

Wei Li is with the Department of Electrical Engineering, Tongji University, Shanghai, 201804, China (e-mail: liweimail@tongji.edu.cn)..

Chang-seop Koh is with the Department of Electrical Engineering, Chungbuk National University, 21366 Cheongju, Korea (e-mail: kohcs@cbnu.ac.kr).

Frede Blaabjerg is with the Department of Energy Engineering, Aalborg University, 9100 Aalborg, Denmark (e-mail: fbl.@et.aau.dk).

Fig. 1. 3-D topology structure of the proposed novel CAP-MLS. (a) Traditional pure PM MLS. (b) Consequent- pole MLS. (c) The proposed CAP-MLS

characteristic of the static thrust force waveform is not good because of its asymmetrical arrangement of PM poles on the mover [9]. This will result in unsmooth operation when the external thrust force fluctuates.

Its thrust and torque characteristics can determine the main performance of an MLS. Thus, thrust and torque calculation and analysis are the main work at the optimal design stage of MLS. Although the finite element analysis (FEA) method is considered and popularly used as one of the most accurate calculation methods of magnetic field for electromagnetic devices [12], The computer consumption is too much for the three-dimensional (3-D) magnetic field analysis [13]-[14]. Especially for the MLS, more quality mesh is needed because of its helical magnetic field distribution in the air gap [15]. The equivalent magnetic circuit (EMC) method is also a traditional analysis method for electromagnetic devices [16]-[20]; however, it is usually applied for two-dimensional (2-D) models, and the model with its parameters needs to update as the state changes in the transient magnetic field analysis. The sub-domain analytical model (AM) has been applied to analyse the MLS performance recently because of its calculation efficiency and accuracy. The accuracy of the subdomain model is high compared to FEA, while the computational speed is far significantly higher [21]-[24]. However, the application is challenging, especially for the complex topology [25].

Compared with the traditional MLS, a novel checkerboard array pole (CAP) MLS is proposed, which can not only save permanent magnet (PM) consumption but also provide enough thrust for application. To save PM consumption, PM and iron teeth are alternately mounted to form a circle of helical magnetic poles on the mover of the proposed CAP-MLS. In addition, the pure PM helical poles are mounted on the rotor to increase the maximum thrust and torque. To analyse the

performance of the proposed CAP-MLS rapidly, a corresponding 3-D sub-domain AM based on the superposition theory is developed. Finally, the proposed novel CAP-MLS topology with its AM is verified through experimental results from a prototype. In this paper, Section II describes the topology and working principle of CAP-MLS. The corresponding 3-D sub-domain AM and its implementation process are proposed in Section III. In Sections IV and V, a 3-D FEA and a prototype are developed, and the results are compared with the proposed 3-D AM to validate the proposed CAP-MLS and its sub-domain AM. Conclusions are made in Section VI.

II. TOPOLOGICAL AND OPERATING PRINCIPLE

The topology structure and pole arrangement of the proposed CAP-MLS are illustrated in Fig. 1 and Fig. 2, respectively. The proposed CAP-MLS consists of two main components: the rotor and the mover. Similar to the traditional MLS, the alternating helical-shaped magnetic poles are mounted on the inner surface of the rotor core, and its axial expanded view is shown in Fig. 2(a). Alternating checkerboard array poles are mounted on the outer surface of the mover core, as shown in Fig. 1, and its axial expanded view is shown in Fig. 2(b). PM and teeth are alternately mounted from the figure to form a spiral magnetic pole circle. Thus, the consumption of PM in the mover pole will be reduced by half.

The operating principle of the proposed CAP-MLS is similar to that of the traditional MLS. The thrust force F of the mover can be transferred to the torque T of the rotor by the helical coupling magnetic field in the air gap between the rotor and the mover, and vice versa.

The relationship between the speed of the mover v and the rotor speed ω follows:

$$\omega \tau_p = 2\pi v \tag{1}$$

Where τ_p indicates the pitch of the MLS pole, as shown in Fig. 3(a).

Neglecting the loss, the rotational output power of the rotor is equal to the linear input power of the mover according to the energy conservation law. The relationship between the mover thrust F and the rotor torque T can be expressed as:

$$T = \frac{v}{\omega} F = \frac{\tau_p}{\pi} F \tag{2}$$

III. A 3-D SUB-DOMAIN ANALYTICAL MODEL FOR THE PROPOSED CAP-MLS

The 2-D section views of planes A and B in Fig. 2(b) are shown in Fig. 3. From the figure, the 2-D sections are quite different between the N and S poles. Therefore, the traditional 2-D analytical model [4], [26] cannot be applied to the proposed CAP-MLS in this paper. Then, a 3-D sub-domain AM [27]-[30] based on the superposition principle is proposed in this paper to analyse the thrust-torque performance of the proposed CAP-

(a)

(b)
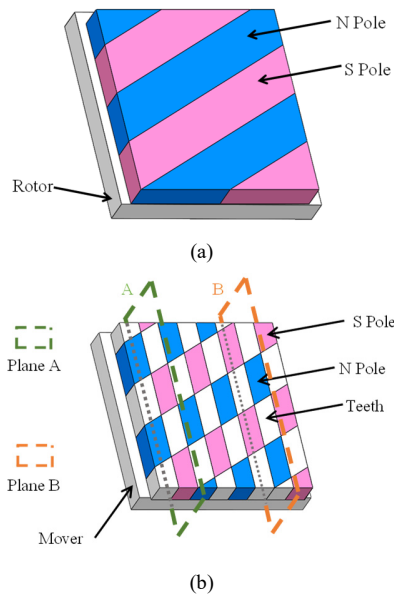
Fig. 2. PMs Array Arrangement. (a) alternating helical-shaped magnetic pole. (b) A novel alternating checkerboard array pole.

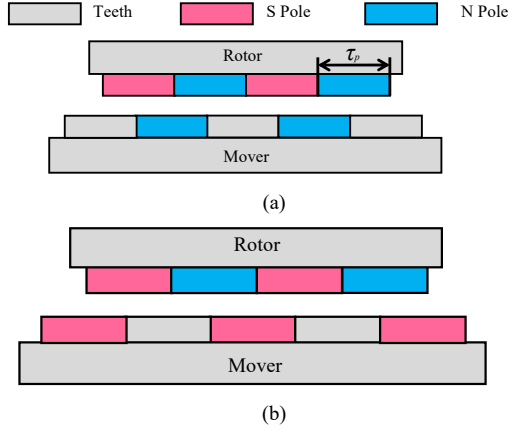> REPLACE THIS LINE WITH YOUR MANUSCRIPT ID NUMBER (DOUBLE-CLICK HERE TO EDIT) <

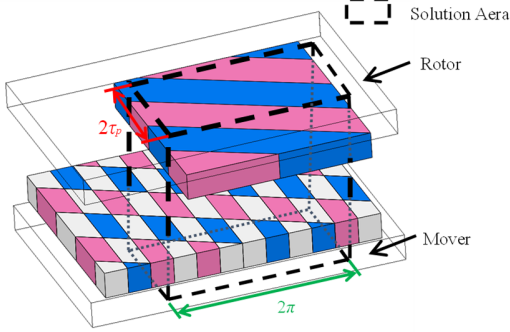Fig. 3. The 2-D section view on the mover. (a) Plane A. (b) Plane B.

Fig. 4. The 3-D analytical Fourier model under the expansion view along the circumferential direction in the θ-z plane.

MLS.

The expansion view of the solution region along the circumferential direction based on the θ-z plane in the proposed sub-domain AM is shown in Fig. 4. The trust force or torque can be generated through the coupling magnetic field in the air gap. And the coupling magnetic field is excitingly generated together by PMs on the rotor and translator. Hence, the air gap coupling magnetic field can be calculated separately between the rotor and translator in the proposed sub-domain AM. Then, they are added together to obtain the total distribution of the air gap magnetic field.

A. Equivalent of the Exciting source

The 2-D view of the PM arrangement on the rotor in the θ-z plane is shown in Fig. 5. According to the figure, the corresponding Fourier expression of the PM poles on the rotor can be expressed as:

$$M_a = \sum_{n=1}^{\infty} \frac{2M_0}{n\pi} \left[1 - \cos(n\pi) \right] \sin\left(\frac{n\pi}{2} \right) \cos\left[np\theta - \frac{n\pi}{\tau_p}(z - \alpha) \right] \quad (3)$$

$$M_0 = B_{rem} / \mu_0 \quad (4)$$

Where M_a represents the remanent magnetization distribution of the rotor remanent magnetization.

The 2-D view of the PM arrangement on the mover in the θ-z plane is shown in Fig. 6. To simplify the 3-D AM, the 2-D view of the CAP on the mover can be equivalently considered as the superposition of two types of topologies, which are single helical pole and magnetic gear pole, as shown in Fig. 7, respectively. Therefore, the Fourier expression of the proposed

CAP topology on the mover can be expressed as follows by using the superposition equivalent method:

$$M_{ca} = M_b - M_c \quad (5)$$

$$M_b = \frac{M_0}{2} + \sum_{l=1}^{\infty} \frac{2M_0}{l\pi} \sin\left(\frac{l\pi}{2} \right) \cos\left[l\theta - \frac{l\pi}{\tau_p}(z - \beta) \right] \quad (6)$$

$$M_c = \frac{M_0}{2} + \sum_{m=1}^{\infty} \frac{2M_0}{m\pi} \sin\left(k_m \frac{\tau_p}{2} \right) \cos(4m\theta) \quad (7)$$

Where M_b represents the remanent magnetization distribution of the single helical pole remanent magnetization. Where M_c represents the remanent magnetization distribution of the magnetic gear pole remanent magnetization. Where M_{ca} represents the remanent magnetization distribution of the mover remanent magnetization. Where n, l, m are the harmonic orders of different subdomains

The remanence distribution results are compared between the actual CAP topology and superposition equivalent model in Fig. 8. From the results, the remanence distribution of the superposition equivalent model is the same as that of the actual CAP topology. It means that the superposition equivalent model of CAP can be applied to the sub-domain model to express the remanence distribution of the proposed CAP topology.

B. The proposed 3-D Analytical Model

As shown in Fig. 9, based on the PM source superposition equivalent method, the proposed 3-D sub-domain AM for the CAP-MLS consists of three models: the rotor model, the single helical model, and the magnetic gear model.

In the case of the rotor model, PMs on the translator are removed. The rotor model is divided into two regions: air gap region (region I$_a$) and PM region (Region II$_a$), as shown in Fig. 9(a). In the case of the translator, the single helical model and magnetic gear model also consist of the air gap region (Region I$_b$ or Region I$_c$) and PM region (Region II$_b$ or Region II$_c$), as shown in Fig. 9(b) and Fig. 9(c), respectively. In the figure, R_1, R_2, R_3 and R_4 indicate the boundary radii of
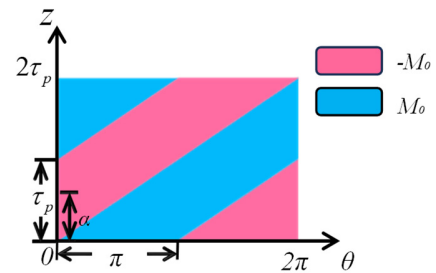

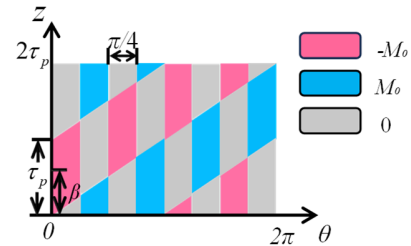**Fig. 5**. The 2-D view of the PM arrangement on the rotor in the θ-z plane.

Fig. 6. The 2-D view of the PM arrangement on the mover in the θ-z plane.
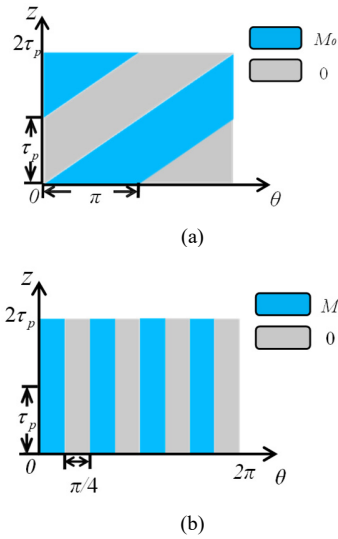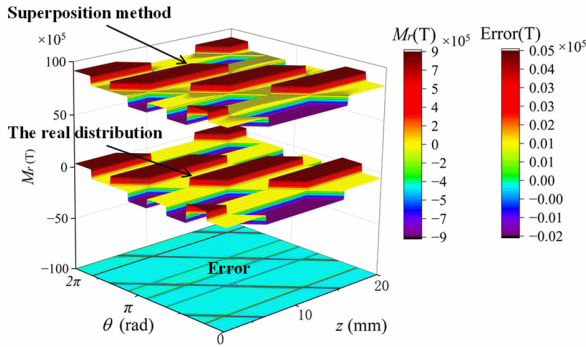
(a)

(b)

Fig. 7. Distribution of the excitation of the two equivalent topologies in the θ-z plane. (a) single helical pole. (b) magnetic gear pole.

the four regions.

Based on the assumption of infinite permeability of back irons and the neglection of the end effect, the governing equations of the proposed sub-domain AM are:

$$\begin{cases} \nabla^2 \varphi_i^{\mathrm{I}} = 0 & (i = a,b,c) \\ \nabla^2 \varphi_i^{\mathrm{II}} = \nabla \cdot M^i / \mu_r & (i = a,b,c) \end{cases} \quad (8)$$

where φ is the defined magnetic scalar potential, μ_r is the relative magnetic permeability of the PM for rotors and translators, and M is the magnetization intensity. Moreover, the proposed checkerboard structure of the magnetic screw with PMs mounted on it is radially magnetized. Thus, M has only a radial component, $M = \{M_I, 0, 0\}$. M_I denotes the radial component of the remanent magnetization of PMs for the rotor and translator.

The magnetic field distribution in terms of the magnetic field intensity H can be described by a magnetic scalar potential φ as:

$$H = -\nabla \varphi \quad (9)$$

The relationship between the magnetic flux density B and magnetic field intensity H can be expressed as:

$$\begin{cases} B_i^{\mathrm{I}} = \mu_0 \mu_r H_i^{\mathrm{I}} & (i = a,b,c) \\ B_i^{\mathrm{II}} = \mu_0 \mu_r H_i^{\mathrm{II}} + \mu_0 M_i^{\mathrm{II}} & (i = a,b,c) \end{cases} \quad (10)$$

where μ_0 is the vacuum magnetic permeability. By combining (8)~(10), the distribution of B with the corresponding solution of φ can be obtained.

In the case of the rotor model, the boundary conditions are:

$$H_{a,z}^{\mathrm{I}} = 0 \big|_{r=R_1} \quad (11)$$

$$B_{a,r}^{\mathrm{II}} = B_{a,r}^{\mathrm{I}} \big|_{r=R_5} \quad (12)$$

$$H_{a,z}^{\mathrm{I}} = H_{a,z}^{\mathrm{II}} \big|_{r=R_3} \quad (13)$$

$$H_{a,z}^{\mathrm{II}} = 0 \big|_{r=R_4} \quad (14)$$

Where $B_{a,r}^{\mathrm{I}}$ and $H_{a,z}^{\mathrm{I}}$ are the radial components of B and axial components of H of region I in the rotor structure, $B_{a,r}^{\mathrm{II}}$ and $H_{a,z}^{\mathrm{II}}$ are the radial components of B and axial components of H of region II in the rotor structure.

In the case of the single helix structure model, the boundary conditions are:

$$H_{b,z}^{\mathrm{II}} = 0 \big|_{r=R_1} \quad (15)$$

$$B_{b,r}^{\mathrm{II}} = B_{b,r}^{\mathrm{I}} \big|_{r=R_2} \quad (16)$$

$$H_{b,z}^{\mathrm{I}} = H_{b,z}^{\mathrm{II}} \big|_{r=R_2} \quad (17)$$

$$H_{b,z}^{\mathrm{II}} = 0 \big|_{r=R_4} \quad (18)$$

Where $B_{a,r}^{\mathrm{I}}$ and $H_{a,z}^{\mathrm{I}}$ are the radial components of B and axial components of H of region I in the rotor structure, $B_{a,r}^{\mathrm{II}}$ and $H_{a,z}^{\mathrm{II}}$ are the radial components of B and axial components of H of region II in the rotor structure.

In the case of the magnetic gear model, the boundary conditions are:

$$H_{c,\theta}^{\mathrm{II}} = 0 \big|_{r=R_1} \quad (19)$$

$$B_{c,r}^{\mathrm{I}} = B_{c,r}^{\mathrm{II}} \big|_{r=R_2} \quad (20)$$

$$H_{c,\theta}^{\mathrm{I}} = H_{c,\theta}^{\mathrm{II}} \big|_{r=R_2} \quad (21)$$

$$H_{c,\theta}^{\mathrm{I}} = 0 \big|_{r=R_4} \quad (22)$$

Where $B_{c,r}^{\mathrm{I}}$ and $H_{c,\theta}^{\mathrm{I}}$ are the radial components of B and circumferential component of H of region I in the magnetic gear model, $B_{c,r}^{\mathrm{II}}$ and $H_{c,\theta}^{\mathrm{II}}$ are the radial components of B and circumferential component of H of region II in the magnetic gear model.

C. Airgap Flux Density

With the expression of remanent magnetization M_r equations (3) ~(7) mentioned above, governing equations(8) can be solved and leads to the expression of magnetic scalar potential φ as (29)~(34) at the bottom of this page, a_n^{I}, b_n^{I}, c_n^{I}, d_n^{I}, a_m^{I}, b_m^{I}, c_m^{I}, d_m^{I}, a_l^{I}, b_l^{I}, c_l^{I}, d_l^{I}, a_n^{II}, b_n^{II}, c_n^{II}, d_n^{II}, a_m^{II}, b_m^{II}, c_m^{II}, d_m^{II}, a_l^{II}, b_l^{II}, c_l^{II} and d_l^{II} are the unknown coefficient solved by boundary conditions. And $\Gamma_{i,k}^{\mathrm{II}}$ ($k=1,2$) are special solutions given in the appendix.

In order to solve for the above unknowns, equations (36) to (44) are brought into equations (11) to (22), the $B_{a,r}^{\mathrm{I}}$, $B_{a,\theta}^{\mathrm{I}}$, $B_{a,z}^{\mathrm{I}}$, $B_{b,r}^{\mathrm{I}}$, $B_{b,\theta}^{\mathrm{I}}$, $B_{b,z}^{\mathrm{I}}$, $B_{c,r}^{\mathrm{I}}$, $B_{c,\theta}^{\mathrm{I}}$, are obtained, the expression for B is written on the next page.

> REPLACE THIS LINE WITH YOUR MANUSCRIPT ID NUMBER (DOUBLE-CLICK HERE TO EDIT) <

The magnetic density in the air gap of CAP-MLS, according to the superposition theorem, can be expressed as:

$$B_r^{\mathrm{I}} = B_{a,r}^{\mathrm{I}} + B_{b,r}^{\mathrm{I}} - B_{c,r}^{\mathrm{I}} \tag{23}$$

$$B_\theta^{\mathrm{I}} = B_{a,\theta}^{\mathrm{I}} + B_{b,\theta}^{\mathrm{I}} - B_{c,\theta}^{\mathrm{I}} \tag{24}$$

$$B_z^{\mathrm{I}} = B_{a,z}^{\mathrm{I}} + B_{b,z}^{\mathrm{I}} \tag{25}$$

D. Thrust force and Torque

Thrust force and torque are two important quantities to evaluate the performance of the novel CAP-MLS. According to the MAXWELL tensor method and the superposition method, the thrust force and torque of the CAP-MLS can be expressed as [26]:

$$F_t = \frac{R_a}{\mu_0} \int_0^{l_z} \int_0^{2\pi} B_r^{\mathrm{I}}(R_a,\theta,z) B_z^{\mathrm{I}}(R_a,\theta,z) d\theta dz \tag{26}$$

$$T_r = \frac{R_a^2}{\mu_0} \int_0^{l_z} \int_0^{2\pi} B_r^{\mathrm{I}}(R_a,\theta,z) B_\theta^{\mathrm{I}}(R_a,\theta,z) d\theta dz \tag{27}$$

$$R_a = (R_2 + R_3)/2 \tag{28}$$

where R_a represents the average radius of the air gap.

E. Implementation Process

The specific implementation process of the proposed 3-D AM model for the proposed CAP-MLS is as follows:

Step 1: Determine the dimensional parameters of the CAP-MLS;

Step 2: Discrete the motion Solve the Fourier series of remanent magnetization distribution by (3)~(7) for the three structures proposed above, respectively;
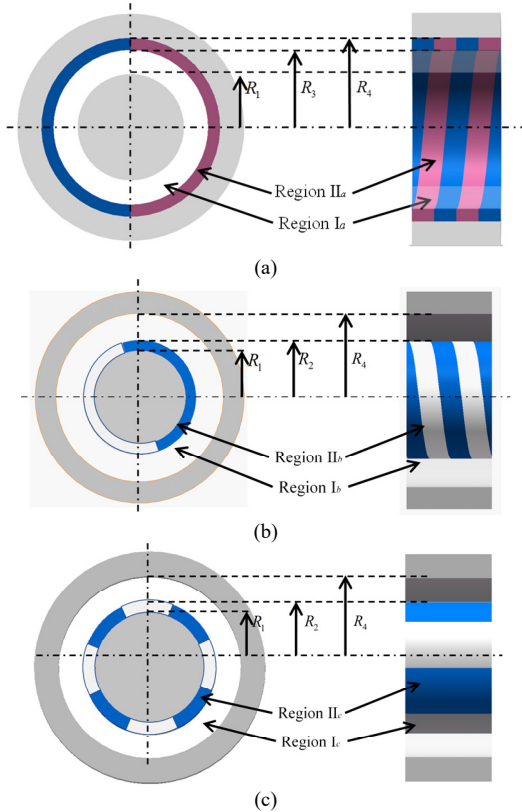

(a)

(b)

(c)

Fig.9. The proposed 3-D sub-domain AM for the CAP-MLS consists of their model. (a) Rotor model. (b) Single helical model. (c) Magnetic gear model.
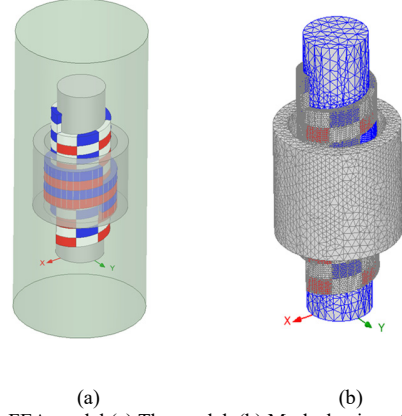

(a)   (b)

Fig. 10. The FEA model (a) The model. (b) Mesh shaving of the model.

Step 3: Solve the special solutions $\Gamma_{a,1}^{\mathrm{II}}$, $\Gamma_{b,1}^{\mathrm{II}}$, $\Gamma_{c,1}^{\mathrm{II}}$, $\Gamma_{a,2}^{\mathrm{II}}$, $\Gamma_{b,2}^{\mathrm{II}}$, $\Gamma_{c,2}^{\mathrm{II}}$ according to the governing equation (8);

Step 4: Find the unknowns according to the boundary conditions (11) to (22);

Step 5: Solve the magnetic densities of the three structures in the air gap separately in (30) to (44).

Step 6: Superposition of the derived magnetic densities to obtain the magnetic densities at the same position in the air gap of the CAP-MLS by (23) to (25).

Step 7: Solve force performance functions (26) and (28).

III. FEA VALIDATION AND PERFORMANCE ANALYSIS

A 3-D FEA model is built to verify the effectiveness and accuracy of the proposed 3-D semi-analytical model for the novel CAP-MLS, shown in Fig. 10. The specification of the verified model is shown in Table I.

The time consumption of 3-D FEA and 3-D AM are 291 minutes and 14 seconds with the CPU i5-13450hx (4.6 GHz), RAM 32GB, respectively. It is shown that the proposed 3-D AM can greatly save computer consumption.

The comparison results of **B** in airgap between the proposed 3-D sub-domain AM and 3-D FEA at $\theta = \pi/8$ and $11\pi/8$ when $\alpha = 0$ and $\beta = \tau_p/2$ are shown in Fig. 11 and 12, respectively. To evaluate the accuracy, the deviation between the proposed AM and FEA results, $d_{B,k}$, is defined as follows:

TABLE I
MAIN PARAMETERS OF CAP-MLS

Symbol	Parameters	Values
R_1	Inner radius of mover PM	22 (mm)
R_2	Outer radius of mover PM	27 (mm)
R_3	Inner radius of rotor PM	28 (mm)
R_4	Outer radius of rotor PM	33 (mm)
Ra	Average airgap radius	27.5(mm)
R_6	Outer diameter of rotor PM	60 (mm)
τ_p	Pole pitch	10 (mm)
l_z	Axial width of the coupling area	20 (mm)
B_r	Magnet remanence	1.2 (T)
μ_0	Vacuum permeability	$4\pi\times10^{-7}$ (N·A^{-2})
μ_r	Magnet relative permeability	1.06
l_r	Effective length of the rotor	40(mm)
l	Effective length of the mover	800 (mm)

> REPLACE THIS LINE WITH YOUR MANUSCRIPT ID NUMBER (DOUBLE-CLICK HERE TO EDIT) <

(a)

(b)

(c)
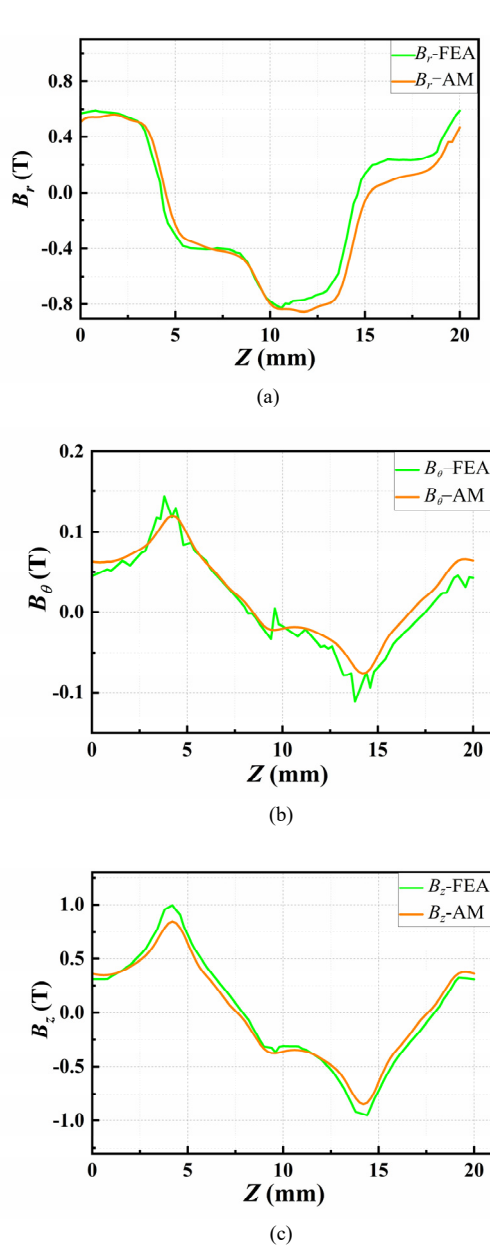
Fig. 11. Distribution of B comparisons by the AM and FEA for the CAP-MLS at $\theta = \pi/8$ when $\alpha = 0$ and $\beta = \tau_p/2$. (a) the radial component B_r of B. (b) the circumferential component B_θ of B. (c) The axial component B_z of B.

$$d_{B,k} = \frac{\sqrt{\sum_{i=1}^{N}\left(B_k^{AM}(i) - B_k^{FEM}(i)\right)^2}}{N \cdot \left\{\max(B_k^{FEM}) - \min(B_k^{FEM})\right\}} \times 100\% \qquad (29)$$

TABLE II
THE SPECIFICATION OF THE HOLE

Symbol	Parameters	Values
d_1	Diameter of PM penetration hole(mm)	3.4
d_2	Diameter of PM surface hole(mm)	6.6
h_1	Connection depth of PM surface hole(mm)	1.6
h_2	Depth of PM hole (mm)	5
r_a	Outer diameter of rotor PM	3.3

(a)

(b)

(c)
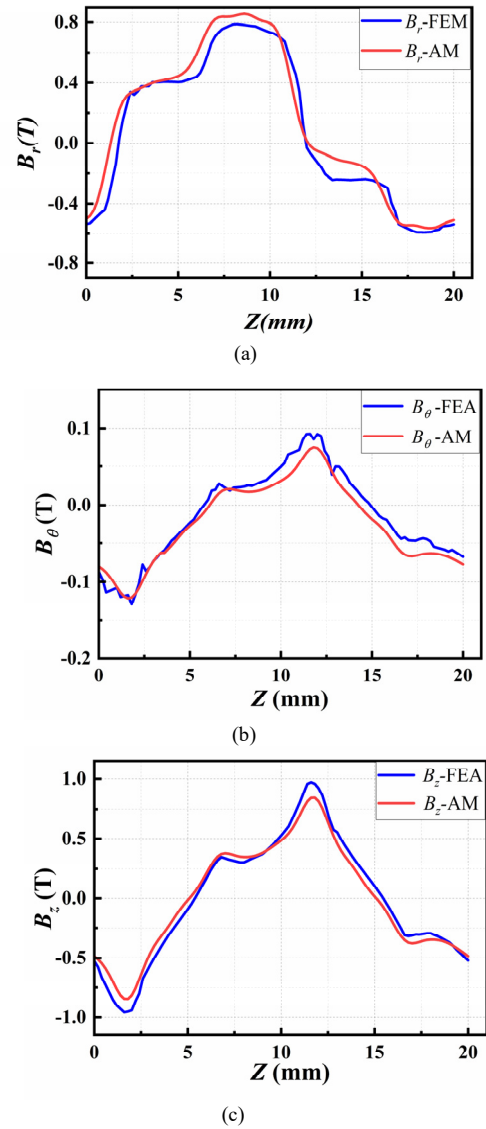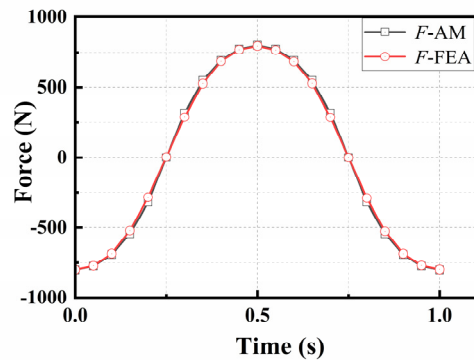
Fig. 12. Distribution of B comparisons by the AM and FEA for the CAP-MLS at $\theta = 11\pi/8$ when $\alpha = 0$ and $\beta = \tau_p/2$ (a) the Radial component of B. (b) the circumferential component of B.(c) The axial component of B.

Fig. 13 The comparison results of force.

where k refers $\underline{r}$, θ, and a. N is the number of sampling points of a B-waveform. The comparison results of $d_{B,k}$ are listed in Table III. From the results, the proposed sub-domain AM and FEA are matched well.

> REPLACE THIS LINE WITH YOUR MANUSCRIPT ID NUMBER (DOUBLE-CLICK HERE TO EDIT) <

The static thrust and torque curves are compared using the two methods, which are shown in Fig. 13 and Fig. 14, respectively. The results show that both the static curves of thrust and torque from the proposed sub-domain analytical method are matched well with that of the FEA model. From the curves, both the static thrust and torque are axisymmetric sinusoidal. And the thrust force and torque deviations, d_{thrust} and d_{torque}, between the proposed AM and FEA are 2.63% and 2.38%, respectively.

The proposed sub-domain AM is also verified with FEA when the structure parameters are different. The comparison results are shown in Fig. 15. From the results, most of the results from the proposed AM match well with those from FEM.

The comparison of the PM utilization rate between the proposed CAP-MLS and traditional pure PM MLS is shown in Fig. 16. From the figure, the PM utility is almost the same when the length of the mover is over 0.5m. The proposed CAP-MLS consumes half the amount of PM compared to the traditional pure PM MLS at the same utilization rate.

IV. EXPERIMENT VERIFICATION

A. Experimental Prototypes and Test Platforms

In this paper, a prototype and testbench of the proposed CAP-MLS are developed and shown in Fig. 18 to validate the performance of the proposed CAP-MLS and its 3-D sub-domain AM. The specifications of the prototype are shown in Table I. In the test bench, an electric cylinder drives the translator of the proposed CAP-MLS, and the translator and rotor are supported by a linear slide and a bearing, respectively. A locker can fix the rotor to measure the static thrust and torque curve.

$$\varphi_a^{\text{I}} = \sum_{n=1}^{\infty}\left[a_n^{\text{I}}\, I_n\left(m_n r\right)+b_n^{\text{I}}\, K_n\left(m_n r\right)\right]\sin(n\theta-m_n z)+\sum_{n=1}^{\infty}\left[c_n^{\text{I}}\, I_n\left(m_n r\right)+d_n^{\text{I}}\, K_n\left(m_n r\right)\right]\cos(n\theta-m_n z) \tag{30}$$

$$\varphi_b^{\text{I}} = \sum_{l=1}^{\infty}\left[a_l^{\text{I}}\, I_l\left(m_l r\right)+b_l^{\text{I}}\, K_l\left(m_l r\right)\right]\sin(l\theta-m_l z)+\sum_{l=1}^{\infty}\left[c_l^{\text{I}}\, I_l\left(m_l r\right)+d_l^{\text{I}}\, K_l\left(m_l r\right)\right]\cos(l\theta-m_l z) \tag{31}$$

$$\varphi_c^{\text{I}} = \sum_{m=1}^{\infty}(a_m^{\text{I}} r^{4m}+b_m^{\text{I}} r^{-4m})\cos\left(4m\theta\right)+\sum_{m=1}^{\infty}(c_m^{\text{I}} r^{4m}+d_m^{\text{I}} r^{-4m})\sin\left(4m\theta\right) \tag{32}$$

$$\varphi_a^{\text{II}} = \sum_{n=1}^{\infty}\left[a_n^{\text{II}}\, I_n\left(m_n r\right)+b_n^{\text{II}}\, K_n\left(m_n r\right)+\Gamma_{a,1}^{\text{II}}\right]\sin(n\theta-m_n z)+\sum_{n=1}^{\infty}\left[c_n^{\text{II}}\, I_n\left(m_n r\right)+d_n^{\text{II}}\, K_n\left(m_n r\right)+\Gamma_{a,2}^{\text{II}}\right]\cos(n\theta-m_n z) \tag{33}$$

$$\varphi_b^{\text{II}} = \sum_{l=1}^{\infty}\left[a_l^{\text{II}}\, I_l\left(m_l r\right)+b_l^{\text{II}}\, K_l\left(m_l r\right)+\Gamma_{b,1}^{\text{II}}\right]\sin(l\theta-m_l z)+\sum_{l=1}^{\infty}\left[c_l^{\text{II}}\, I_l\left(m_l r\right)+d_l^{\text{II}}\, K_l\left(m_l r\right)+\Gamma_{b,2}^{\text{II}}\right]\cos(l\theta-m_l z) \tag{34}$$

$$\varphi_c^{\text{II}} = \sum_{m=1}^{\infty}(a_m^{\text{II}} r^{4m}+b_m^{\text{II}} r^{-4m}+\Gamma_{c,1}^{\text{II}})\sin\left(4m\theta\right)+\sum_{m=1}^{\infty}(c_m^{\text{II}} r^{4m}+d_m^{\text{II}} r^{-4m}+\Gamma_{c,2}^{\text{II}})\cos\left(4m\theta\right) \tag{35}$$

$$B_{a,r}^{\text{I}} = \sum_{n=1}^{\infty}\mu_0 m_n\left[-a_n^{\text{I}}\, I_n'\left(m_n r\right)-b_n^{\text{I}}\, K_n'\left(m_n r\right)\right]\sin\left(n\theta-m_n z\right)+\sum_{n=1}^{\infty}\mu_0 m_n\left[-c_n^{\text{I}}\, I_n'\left(m_n r\right)-d_n^{\text{I}}\, K_n'\left(m_n r\right)\right]\cos\left(n\theta-m_n z\right) \tag{36}$$

$$B_{a,\theta}^{\text{I}} = \frac{\mu_0}{r}\left\{\left[\sum_{n=1}^{\infty}-na_n^{\text{I}}\, I_n\left(m_n r\right)+nb_n^{\text{I}}\, K_n\left(m_n r\right)\right]\cos\left(n\theta-m_n z\right)+\left[\sum_{n=1}^{\infty}-nc_n^{\text{I}}\, I_n\left(m_n r\right)+nd_n^{\text{I}}\, K_n\left(m_n r\right)\right]\sin\left(n\theta-m_n z\right)\right\} \tag{37}$$

$$B_{a,z}^{\text{I}} = \mu_0\left\{\sum_{n=1}^{\infty} m_n\left[a_n^{\text{I}}\, I_n\left(m_n r\right)+b_n^{\text{I}}\, K_n\left(m_n r\right)\right]\cos\left(n\theta-m_n z\right)-\sum_{n=1}^{\infty} m_n\left[c_n^{\text{I}}\, I_n\left(m_n r\right)+d_n^{\text{I}}\, K_n\left(m_n r\right)\right]\sin\left(n\theta-m_n z\right)\right\} \tag{38}$$

$$B_{b,r}^{\text{I}} = \sum_{l=1}^{\infty}\mu_0 m_l\left[-a_l^{\text{I}}\, I_l'\left(m_l r\right)-b_l^{\text{I}}\, K_l'\left(m_l r\right)\right]\sin\left(l\theta-m_l z\right)+\sum_{l=1}^{\infty}\mu_0 m_l\left[-c_l^{\text{I}}\, I_l'\left(m_l r\right)-d_l^{\text{I}}\, K_l'\left(m_l r\right)\right]\cos\left(l\theta-m_l z\right) \tag{39}$$

$$B_{b,\theta}^{\text{I}} = \frac{\mu_0}{r}\left\{\left[\sum_{l=1}^{\infty}-la_l^{\text{I}}\, I_l\left(m_l r\right)+lb_l^{\text{I}}\, K_l\left(m_l r\right)\right]\cos\left(l\theta-m_l z\right)+\left[\sum_{l=1}^{\infty}-lc_l^{\text{I}}\, I_l\left(m_l r\right)+ld_l^{\text{I}}\, K_l\left(m_l r\right)\right]\sin\left(l\theta-m_l z\right)\right\} \tag{40}$$

$$B_{b,z}^{\text{I}} = \mu_0\left\{\sum_{l=1}^{\infty} m_l\left[a_l^{\text{I}}\, I_l\left(m_l r\right)+b_l^{\text{I}}\, K_l\left(m_l r\right)\right]\cos\left(l\theta-m_l z\right)-\sum_{l=1}^{\infty} m_l\left[c_l^{\text{I}}\, I_l\left(m_l r\right)+d_l^{\text{I}}\, K_l\left(m_l r\right)\right]\sin\left(l\theta-m_l z\right)\right\} \tag{41}$$

$$B_{c,r}^{\text{I}} = -\mu_0\left[\sum_{m=1}^{\infty}\left(a_m^{\text{I}}\, 4mr^{4m-1}-b_m^{\text{I}}\, 4mr^{-4m-1}\right)\sin\left(4m\theta\right)+\sum_{m=1}^{\infty}\left(c_m^{\text{I}}\, 4mr^{4m-1}-d_m^{\text{I}}\, 4mr^{-4m-1}\right)\cos\left(4m\theta\right)\right] \tag{42}$$

$$B_{c,\theta}^{\text{I}} = -\mu_0\left[\sum_{m=1}^{\infty} 4m\left(a_m^{\text{I}} r^{4m}-b_m^{\text{I}} r^{-4m}\right)\cos\left(4m\theta\right)-\sum_{m=1}^{\infty}\left(c_m^{\text{I}} r^{4m}-d_m^{\text{I}} r^{-4m}\right)\sin\left(4m\theta\right)\right] \tag{43}$$

$$m_n = \frac{n\pi}{\tau_p},\, m_l = \frac{l\pi}{\tau_p} \tag{44}$$
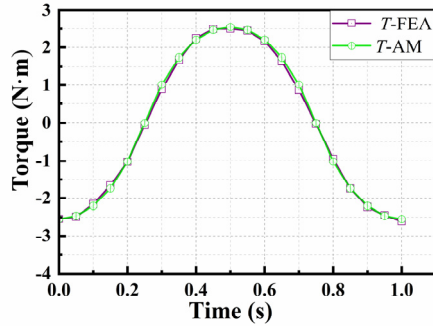
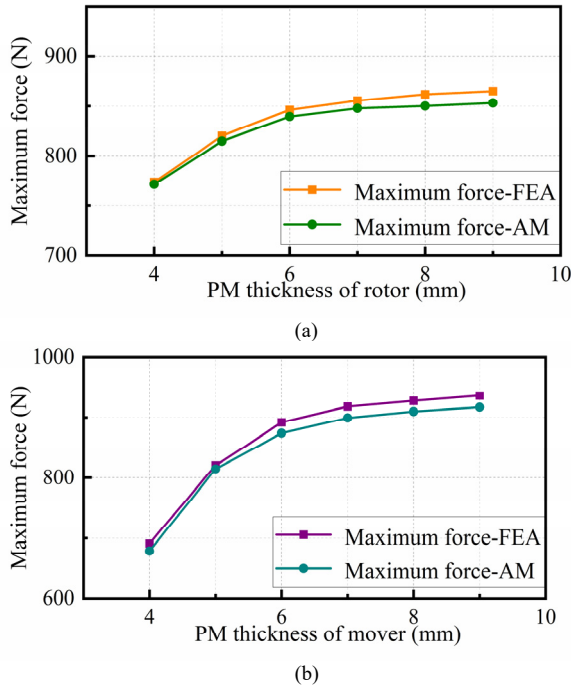**Fig. 14.** The comparison results of torque.

(a)

(b)

Fig. 15. Comparison results between the proposed sub-domain AM and FEM when the structure parameters are different. (a) PM thickness of the rotor. (b) PM thickness of mover.
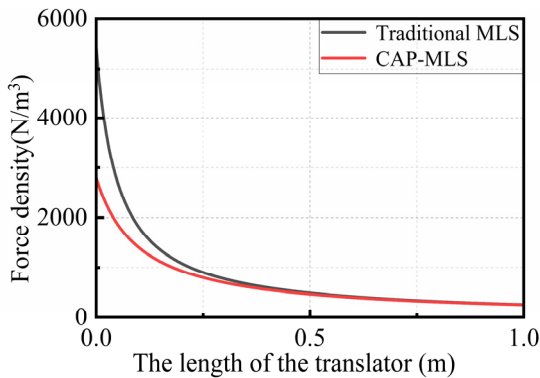

Fig. 16. The comparison of the PM utilization rate between the proposed CAP-MLS and traditional pure PM MLS.

The manufacture of a helical-shaped PM pole is very hard and expensive. In literature [31], the spiral segments on the MLS were made into circular PMs segments to facilitate the installation of the MLS. Therefore, MLS without translation

tilt is proposed in [32]. This translator uses a ring structure instead of an inclined structure, which reduces the difficulty of
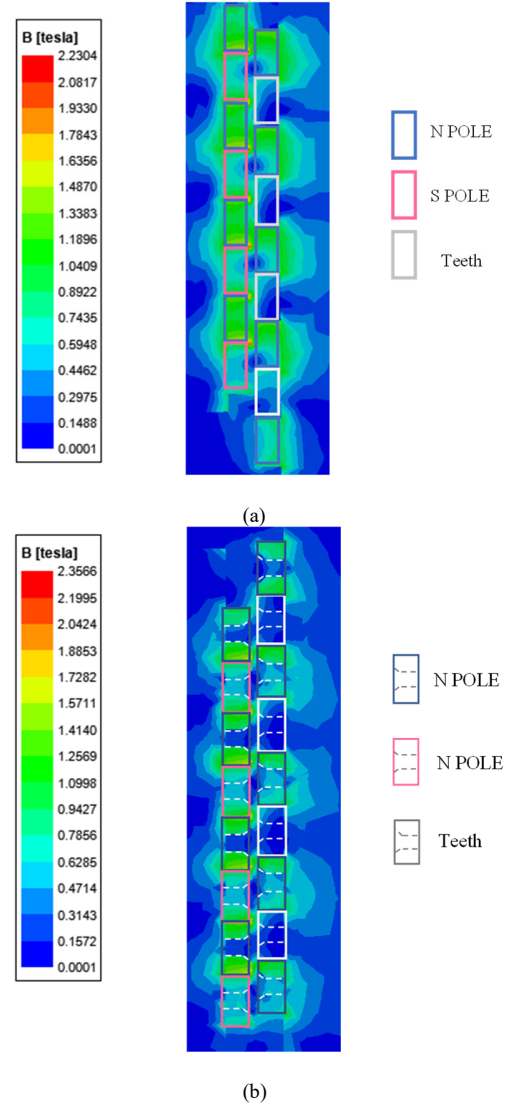

(a)

(b)

Fig. 17. The magnetic flux density distribution comparison results on the hole effect, which is about the plane A through the center of the hole shown in Fig. 2. (a) The tradition PM segments are without holes. (b) The proposed PM segments drilled holes.

TABLE III
THE ACCURACY COMPARISON BETWEEN
THE PROPOSED AM AND FEM

Symbol	$\theta = \pi/8$	$\theta = 11\pi/8$
$d_{B,r}$	7.211%	7.255%
$d_{B,\theta}$	5.811%	6.216%
$d_{B,z}$	3.779%	3.983%

manufacturing MLS. A segmentation joint method is used in this paper to generate a near-ideal helical PM pole. The generated magnetic field in the air gap is closest to the helical shape when the minimum segment number is eight [6]. Therefore, a cycle of the helical PM pole is divided into eight segments in this paper, the PM and teeth segment are

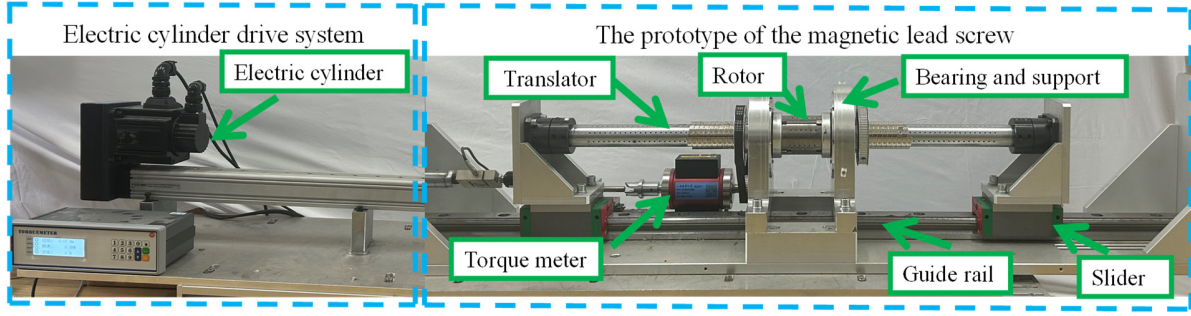> REPLACE THIS LINE WITH YOUR MANUSCRIPT ID NUMBER (DOUBLE-CLICK HERE TO EDIT) <

Fig. 20. Translator and rotor of the CAP-MLS. (a) Translator fragment. (b) Rotor fragment.

alternately arranged to generate the checkerboard array PM. The single PM segment and the jointed helical PM poles are shown in Fig. 18 and Fig. 19, respectively.

Usually, the PM segments are fixed to the rotor and translator surfaces by special glue [31]. Although it performs well, the uncontrollable glue thickness can lead to uneven air gaps and even collisions between the mover and rotor. To guarantee the width of the airgap is uniform, a new PM segment installation method using bolts is adopted in this paper, with the PMs and teeth as shown in Fig. 19. By using this amount method, not only the width of airgap can be uniform, but also the PM segment can be conveniently

Fig. 18. Proposed novel magnet and teeth segments on the translator. (a) Magnet segment. (b) The segment with teeth.

Fig. 19. Translator and rotor of the CAP-MLS. (a) Translator fragment. (b) Rotor fragment.

replaced once damaged. The helical PM pole on the rotor and mover consists of 8 spiral permanent magnet segments. the relevant parameters of the screw holes on it are shown in Table II. The magnetic flux density distribution comparison results on the hole effect are shown in Fig. 17, which is about plane A through the center of the hole shown in Fig. 2. From the results, the flux density distribution on the PM segment of the mover and rotor changes when the holes are drilled. And the saturation effect does not appear. It means the PM is fully utilized.

By considering the drilled hole on the PM segments, whose radius is 3.3 mm in this prototype, the trust F^* and torque T^* in the proposed sub-domain AM can be expressed as:

$$F^* = k_a F_t \qquad (45)$$

$$T^* = k_a T_r \qquad (46)$$

Where k_a is the force attenuation coefficient, which can be expressed as:

$$k_a = (S_c - S_h)/S_c = 1 - \frac{N_s r_a^2}{2 R_a \tau_p} \qquad (47)$$

where S_h is the sum of the surface areas of all holes in the coupling region, N_s is the number of PM segments for one turn on a helix, and r_a is the radius of the hole on the surface.

The rotor can rotate by driving the translator back and forth horizontally through the electric cylinder. The torque can be measured by a torque meter connected to the rotor by a belt, as shown in Fig 18. Simultaneously, the thrust can also be measured by a force meter installed between the prototype and the electric cylinder, as shown in Fig. 18. The static thrust and torque curves can be measured when the locker locks the rotor. The measured static thrust and torque curves are shown in Fig. 18, respectively. The deviation d_{thrust}^{mea} and d_{torque}^{mea} between the proposed AM and measured results are 1.651% and 1.669%, respectively. The curves from the two methods matched well with the compared results. The thrust and torque curves have good symmetry characteristics about the pole centerline.

The thrust force for the model with PM holes is compared between the proposed sub-domain AM and FEA when the radius of the holes is different, as shown in Fig. 22. From the results, the thrust after attenuation in (47) is match well with that of FEA. In addition, From the figure, the smaller the hole radius, the greater the thrust. However, it is also necessary to comprehensively consider the process level of the opening to determine the size of the hole radius.
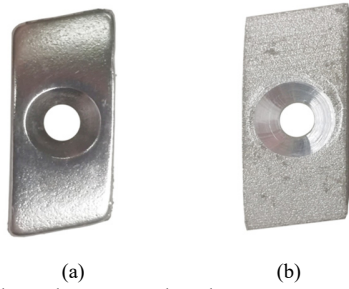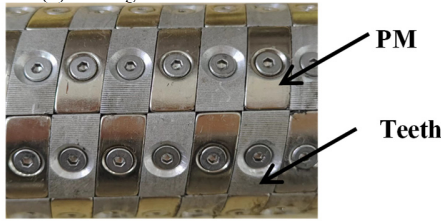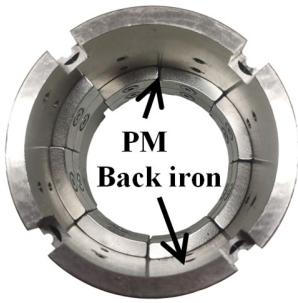
(a)

(b)
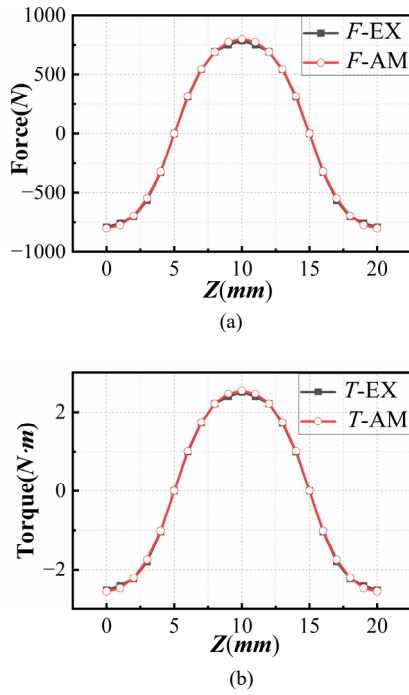
Fig. 21. Comparison of experimental measurements with AM calculations. (a) Force. (b) Torque.
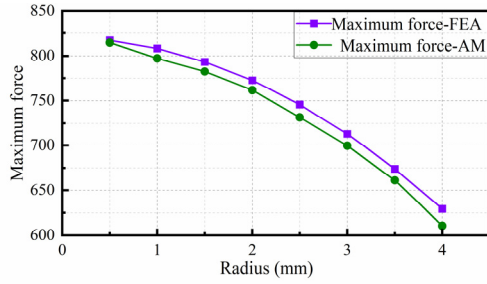
Fig. 22. The thrust force for the model with PM holes is compared between the proposed sub-domain AM and FEA when the radius of the holes is different.

APPENDIX

$$\Gamma_{a,1}^{\text{II}} = f_{1a}\left(m_n r\right) I_n\left(m_n r\right) + f_{2a}\left(m_n r\right) K_n\left(m_n r\right) \tag{A1}$$

$$\Gamma_{a,2}^{\text{II}} = f_{3a}\left(m_n r\right) I_n\left(m_n r\right) + f_{4a}\left(m_n r\right) K_n\left(m_n r\right) \tag{A2}$$

$$\Gamma_{b,1}^{\text{II}} = g_{1a}\left(m_l r\right) I_l\left(m_l r\right) + g_{2a}\left(m_l r\right) K_l\left(m_l r\right) \tag{A3}$$

$$\Gamma_{b,2}^{\text{II}} = g_{3a}\left(m_l r\right) I_l\left(m_l r\right) + g_{4a}\left(m_l r\right) K_l\left(m_l r\right) \tag{A4}$$

$$\Gamma_{c,1}^{\text{II}} = u_{1c}\left(r\right) r^{4m} + u_{2c}\left(r\right) r^{-4m} \tag{A5}$$

$$\Gamma_{c,2}^{\text{II}} = u_{3c}\left(r\right) r^{4m} + u_{4c}\left(r\right) r^{-4m} \tag{A6}$$

$$f_{1a}\left(m_n r\right) = -\frac{\frac{2M_0}{n\pi}\left[1-\cos\left(n\pi\right)\right]\sin\left(\frac{n\pi}{2}\right)}{\mu_r m_n}\sin\left(m_n\alpha\right)\int_{m_n R_4}^{m_n r} K_n\left(x\right)dx \tag{A7}$$

$$f_{1a}\left(m_n r\right) = \frac{\frac{2M_0}{n\pi}\left[1-\cos\left(n\pi\right)\right]\sin\left(\frac{n\pi}{2}\right)}{\mu_r m_n}\sin\left(m_n\alpha\right)\int_{m_n R_4}^{m_n r} I_n\left(x\right)dx \tag{A8}$$

$$f_{3a}\left(m_n r\right) = \frac{\frac{2M_0}{n\pi}\left[1-\cos\left(n\pi\right)\right]\sin\left(\frac{n\pi}{2}\right)}{\mu_r m_n}\cos\left(m_n\alpha\right)\int_{m_n R_4}^{m_n r} K_n\left(x\right)dx \tag{A9}$$

$$f_{4a}\left(m_n r\right) = -\frac{\frac{2M_0}{n\pi}\left[1-\cos\left(n\pi\right)\right]\sin\left(\frac{n\pi}{2}\right)}{\mu_r m_n}\cos\left(m_n\alpha\right)\int_{m_n R_4}^{m_n r} I_n\left(x\right)dx \tag{A10}$$

$$g_{1a}\left(m_l r\right) = -\frac{\frac{2M_0}{l\pi}\sin\left(\frac{l\pi}{2}\right)}{\mu_r m_l}\sin\left(m_l\beta\right)\int_{m_l R_1}^{m_l r} K_l\left(x\right)dx \tag{A11}$$

$$g_{2a}\left(m_l r\right) = \frac{\frac{2M_0}{l\pi}\sin\left(\frac{l\pi}{2}\right)}{\mu_r m_l}\sin\left(m_l\beta\right)\int_{m_l R_1}^{m_l r} I_l\left(x\right)dx \tag{A12}$$

$$g_{3a}\left(m_l r\right) = \frac{\frac{2M_0}{l\pi}\sin\left(\frac{l\pi}{2}\right)}{\mu_r m_l}\cos\left(m_l\beta\right)\int_{m_l R_4}^{m_l r} K_l\left(x\right)dx \tag{A13}$$

$$g_{4a}\left(m_l r\right) = -\frac{\frac{2M_0}{l\pi}\sin\left(\frac{l\pi}{2}\right)}{\mu_r m_l}\cos\left(m_l\beta\right)\int_{m_l R_4}^{m_l r} I_l\left(x\right)dx \tag{A14}$$

$$u_{1c} = \frac{2M_0}{m\pi}\sin\left(\frac{m\pi}{2}\right)\sin\left(4m\beta\right)\int_{R_1}^{r}\frac{1}{8mx^{4m-1}}dx \tag{A15}$$

$$u_{2c} = -\frac{2M_0}{m\pi}\sin\left(\frac{m\pi}{2}\right)\sin\left(4m\beta\right)\int_{R_1}^{r}\frac{x^{4m+1}}{8m}dx \tag{A16}$$

$$u_{3c} = \frac{2M_0}{m\pi}\sin\left(\frac{m\pi}{2}\right)\cos\left(4m\beta\right)\int_{R_1}^{r}\frac{1}{8mx^{4m-1}}dx \tag{A17}$$

$$u_{4c} = -\frac{2M_0}{m\pi}\sin\left(\frac{m\pi}{2}\right)\cos\left(4m\beta\right)\int_{R_1}^{r}\frac{x^{4m+1}}{8m}dx \tag{A18}$$

V. CONCLUSION

In this paper, a novel topology of CAP-MLS is proposed to save PM consumption and can obtain a symmetric static trust and torque compared with CP-MLS. Also, a corresponding 3-D sub-domain AM based on the superposition equivalent method is proposed to analyse the magnetic field distribution and performance of trust and torque of the proposed CAP-MLS. The analysis results of the proposed 3-D sub-domain AM are verified by a 3-D FEA model and an experimental prototype. And the analytical results, including waveforms of flux density, thrust force and torque, are all in good agreement with the 3-D FEA model and experimental results. Compared with the FEA model, the proposed 3-D sub-domain AM can significantly reduce the time consumption and accelerate the optimized design process.

REFERENCES

[1] J. Zhang *et al*., "Relative Speed Compensation for Sensorless Control of Magnetic Screw Motor Based on an Improved Pulsating Current Injection Method," in *IEEE Transactions on Transportation Electrification*, doi: 10.1109/TTE.2024.3386979.

[2] J. Zhang, Z. Liu, G. Liu, Q. Chen, J. Jatskevich and C. H. T. Lee, "Fast Response Sliding Mode Linear Speed Control of a Magnetic Screw Motor Based on Feedforward Compensation Strategy," in *IEEE Transactions on Transportation Electrification*, vol. 10, no. 1, pp. 1441-1453, March 2024, doi: 10.1109/TTE.2023.3290396

[3] S. Meng, Z. Ling, W. Zhao, J. Ji, and M. Xu, "Design and analysis of a surface-inserted magnetic screw with minimum thrust force ripple," IEEE Trans. Transport. Electrific., doi: 10.1109/TTE.2024.3349530.

[4] L. Zhu et al., "A Novel Hybrid Excitation Magnetic Lead Screw and Its Transient Sub-Domain Analytical Model for Wave Energy Conversion," in IEEE Transactions on Energy Conversion, doi: 10.1109/TEC.2024.3354512.

[5] Ji, Z. Ling, J. Wang, W. Zhao, G. Liu and T. Zeng, "Design and Analysis of a Halbach Magnetized Magnetic Screw for Artificial Heart," in IEEE Transactions on Magnetics, vol. 51, no. 11, pp. 1-4, Nov. 2015, Art no. 8108604, doi: 10.1109/TMAG.2015.2436691.

[6] Z. Ling, J. Ji, J. Wang and W. Zhao, "Design Optimization and Test of a Radially Magnetized Magnetic Screw With Discretized PMs," in *IEEE Transactions on Industrial Electronics*, vol. 65, no. 9, pp. 7536-7547, Sept. 2018, doi: 10.1109/TIE.2017.2740820.

[7] M. Cirolini, A. F. Flores Filho, Y. C. Wu and D. G. Dorrell, "Design Aspects of a Reluctance-Based Magnetic Lead Screw," in *IEEE Transactions on Magnetics*, vol. 55, no. 7, pp. 1-6, July 2019, Art no. 8001906, doi: 10.1109/TMAG.2019.2895681.

[8] K. Lu and W. Wu, "Electromagnetic Lead Screw for Potential Wave Energy Application," in *IEEE Transactions on Magnetics*, vol. 50, no. 11, pp. 1-4, Nov. 2014, Art no. 8205004, doi: 10.1109/TMAG.2014.2325611.

[9] L. Zhu, Q. Wu, W. Li, W. Wu, C. -S. Koh and F. Blaabjerg, "A Novel Consequent-Pole Magnetic Lead Screw and its 3-D Analytical Model With Experimental Verification for Wave Energy Conversion," in *IEEE Transactions on Energy Conversion*, vol. 39, no. 2, pp. 1202-1215, June 2024, doi: 10.1109/TEC.2023.3331008.

[10] T. Xia, Z. Li, H. Liu, Y. Zhang and H. Yu, "Design of a Magnetic Field Modulated Screw Containing Composite Rotors for Wave Energy Conversion," in *IEEE Transactions on Power Electronics*, doi: 10.1109/TPEL.2024.3424535.

[11] Z. Ling, W. Zhao, Y. Sun, J. Ji and M. Xu, "Characteristic Analysis and Harmonic Function Validation of 3-D Modulation Effect for Magnetic Lead Screw Transmission," in *IEEE Transactions on Transportation Electrification*, doi: 10.1109/TTE.2024.3399749.

[12] F. Li, K. Wang, J. Li and H. Y. Sun, "Electromagnetic Performance Analysis of Consequent-Pole PM Machine With Asymmetric Magnetic Pole," in *IEEE Transactions on Magnetics*, vol. 55, no. 6, pp. 1-5, June 2019, Art no. 8103205, doi: 10.1109/TMAG.2019.2904948.

[13] P. Jin, Y. Tian, Y. Lu, Y. Guo, G. Lei and J. Zhu, "3-D Analytical Magnetic Field Analysis of the Eddy Current Coupling With Halbach Magnets," in IEEE Transactions on Magnetics, vol. 56, no. 1, pp. 1-4, Jan. 2020, Art no. 7501904, doi: 10.1109/TMAG.2019.2950389.

[14] X. Sun, N. Xu, and M. Yao, "Sequential subspace optimization design of a dual three-phase permanent magnet synchronous hub motor based on NSGA III," IEEE Trans. Transport. Electrific., vol. 9, no. 1, pp. 622-630, Mar. 2023.

[15] A. Demenko and J. K. Sykulski, "Analogies Between Finite-Difference and Finite-Element Methods for Scalar and Vector Potential Formulations in Magnetic Field Calculations," in *IEEE Transactions on Magnetics*, vol. 52, no. 6, pp. 1-6, June 2016, Art no. 7004206, doi: 10.1109/TMAG.2016.2521345.

[16] G. D. Mamontov, A. V. Syutkin, A. S. Brilinskiy, I. V. Popov and G. A. Evdokunin, "Determination of Magnetic Equivalent Circuit Parameters of Transformer for Saturation Modes," *2023 Seminar on Electrical Engineering, Automation & Control Systems, Theory and Practical Applications (EEACS)*, Saint Petersburg, Russian Federation, 2023, pp. 231-234, doi: 10.1109/EEACS60421.2023.10397405

[17] X. Zhu, G. Qi, M. Cheng, W. Qin, Y. Liu and J. Huang, "Equivalent Magnetic Network Model of Electrical Machine Based on Three Elements: Magnetic Flux Source, Reluctance and Magductance," in *IEEE Transactions on Transportation Electrification*, doi: 10.1109/TTE.2024.3443521.

[18] S. Wang, F. Chen, Z. Tian, X. Wu and A. Li, "An Enhanced Magnetic Equivalent Circuit Model for a Magnetorheological Clutch Including Nonlinear Permeability, Flux Fringing, and Leakage Effects," in *IEEE Transactions on Transportation Electrification*, vol. 9, no. 1, pp. 488-500, March 2023, doi: 10.1109/TTE.2022.3186514.

[19] Q. Liu *et al.*, "Loss Evaluation of Magnetic Devices Using Cauer Equivalent Circuit Identified From Input Impedance," in *IEEE Transactions on Magnetics*, vol. 60, no. 3, pp. 1-5, March 2024, Art no. 6300305, doi: 10.1109/TMAG.2023.3303880.

[20] X. Ba, Y. Guo, J. Zhu and C. Zhang, "An Equivalent Circuit Model for Predicting the Core Loss in a Claw-Pole Permanent Magnet Motor With Soft Magnetic Composite Core," in *IEEE Transactions on Magnetics*, vol. 54, no. 11, pp. 1-6, Nov. 2018, Art no. 8206706, doi: 10.1109/TMAG.2018.2865406.

[21] M. H. Javanmardi, A. Rahideh and V. Z. Faradonbeh, "Analytical Cogging Torque and Unbalanced Magnetic Force Calculations in Slotted Surface-PM Machines Assuming Finite Iron Permeability," in *IEEE Transactions on Transportation Electrification*, doi: 10.1109/TTE.2024.3365137.

[22] R. Kumar and N. C. Kar, "Sub-Domain Model for Induction Motor With More Accurate Realization of Tooth-Saturation," in *IEEE Transactions on Energy Conversion*, vol. 39, no. 3, pp. 1673-1685, Sept. 2024, doi: 10.1109/TEC.2024.3356988.

[23] J. Hu, F. Liu and Y. Li, "An Improved Sub-Domain Model of Flux Switching Permanent Magnet Machines Considering Harmonic Analysis and Slot Shape," in *IEEE Access*, vol. 9, pp. 55260-55270, 2021, doi: 10.1109/ACCESS.2021.3071792.

[24] K. Yang, F. Zhao, J. Yu, C. Zhang and Y. Wang, "Nonlinear Analytical Model of a Double-Stator Flux Reversal Halbach Array Permanent Magnet Machine," in *IEEE Transactions on Energy Conversion*, vol. 39, no. 1, pp. 493-503, March 2024, doi: 10.1109/TEC.2023.3310656.

[25] F. Gao, Q. Wang and J. Zou, "Analytical Modeling of 3-D Magnetic Field and Performance in Magnetic Lead Screws Accounting for Magnetization Pattern," in *IEEE Transactions on Industrial Electronics*, vol. 67, no. 6, pp. 4785-4796, June 2020, doi: 10.1109/TIE.2019.2931241.

[26] F. Farrokh, A. Vahedi, H. Torkaman, M. Banejad and V. Zamani Faradonbeh, "Fast 2-D Analytical Model for Axial-Field Flux-Switching Bar-Permanent Magnet Motor," in *IEEE Transactions on Magnetics*, vol. 60, no. 8, pp. 1-12, Aug. 2024, Art no. 8201912, doi: 10.1109/TMAG.2024.3416176.

[27] Mollaeian, E. Ghosh, H. Dhulipati, J. Tjong and N. C. Kar, "3-D Sub-Domain Analytical Model to Calculate Magnetic Flux Density in Induction Machines With Semiclosed Slots Under No-Load Condition," in *IEEE Transactions on Magnetics*, vol. 53, no. 6, pp. 1-5, June 2017, Art no. 7206905, doi: 10.1109/TMAG.2017.2658543.

[28] W. Ullah, F. Khan, E. Sulaiman, I. Sami and J. Ro, "Analytical Sub-Domain Model for Magnetic Field Computation in Segmented Permanent Magnet Switched Flux Consequent Pole Machine," in *IEEE Access*, vol. 9, pp. 3774-3783, 2021, doi: 10.1109/ACCESS.2020.3047742.

[29] S. W. Jung *et al.*, "3-D Integrated Sub-Domain Model for On-Load Magnetic Field and Force Analysis of 6-DOF Screw-Motion Permanent Magnet Synchronous Motor," in *IEEE Transactions on Energy Conversion*, vol. 38, no. 4, pp. 2487-2498, Dec. 2023, doi: 10.1109/TEC.2023.3277011

[30] L. Gao, Z. Cai, Y. Liang, D. Wang, Q. Niu and J. Li, "An Improved Analytical Model of Magnetic Field in Surface-Mounted Permanent Magnet Synchronous Motor With Magnetic Pole Cutting," in *IEEE Access*, vol. 9, pp. 142804-142814, 2021, doi: 10.1109/ACCESS.2021.3120205.

[31] W. Li and K. -M. Lee, "Design and Parametric Analysis of a Magnetic Leadscrew With an Embedded Displacement Sensor," in *IEEE/ASME Transactions on Mechatronics*, vol. 28, no. 4, pp. 1797-1806, Aug. 2023, doi: 10.1109/TMECH.2023.3271584.

[32] M. B. Kouhshahi, J. Z. Bird, A. Jannsen, J. Kadel, and W. Williams, "A magnetically geared lead screw without translator skewing," in Proc. IEEE Energy Convers. Congr. Expo., 2018, pp. 4994-4999, doi: 10.1109/ECCE.2018.8557751.